atmosphere

MDPI

Article

River-Induced Anomalies in Seasonal Variation of Traffic-Emitted CO Distribution over the City of Krasnoyarsk

Michael Hrebtov [1,*] and Kemal Hanjalić [2]

[1] Institute of Thermophysics of SB RAS, Lavrentiev Ave. 1, 630090 Novosibirsk, Russia
[2] Chemical Engineering Department, Delft University of Technology, Bld. 58, Van der Maasweg 9, 2629 HZ Delft, The Netherlands
* Correspondence: weexov@ya.ru

Received: 14 June 2019; Accepted: 11 July 2019; Published: 17 July 2019

Abstract: Seasonal variation of air quality in a city with a large river was investigated by means of numerical simulations of air movement and pollutant dispersion over inversion-capped diurnal cycles using a Reynolds-averaged Navier–Stokes (RANS) approach with algebraic turbulent flux model. The study accounts for the effects of urban heat island (UHI), terrain orography and high thermal inertia of the river body. The case mimics the real environment of the Krasnoyarsk region with the river Yenisei (Russia). Two scenarios were considered typical of the winter and summer seasons. The study is focused on the dynamics of dispersion of CO emanating mainly from road traffic, which remains fairly uniform throughout the year. The simulation starts from a mild low-altitude inversion with penetrative convection gradually developing over the daytime and attenuating during the night. The main difference between the two cases is in the temperature of the river surface relative to the ambient air. In winter, the non-freezing river acts as a source of positive thermal buoyancy, while in summer the cool river at the daytime acts in the opposite way, as a heat sink. The effect of the river-induced air circulation appears significant enough to account for the observed winter accumulation of the pollutant in the city center.

Keywords: atmospheric boundary layer; diurnal convection; seasonal variation; pollutants dispersion; Reynolds-averaged Navier–Stokes modelling

1. Introduction

Seasonal variations of air quality in urban and other agglomerations with complex natural and human-made canopies have received considerable attention among the environmental community, e.g., References [1–7]. Next to seasonal variability of local weather conditions and variation of emission density in time and over the terrain, many other factors influence this dynamics: The heights, size and density of buildings, the extent, intensity and dynamics of traffic on urban roadways, and others, making it difficult to explain the observed peculiarities of local seasonal patterns of pollutant concentration and their correlation (or the lack of it), with the dynamics of pollutant emission.

Studies of time variability and seasonal variations—based in most cases on long-term collection of a large amount of measured airborne concentrations of representative, and/or specific pollutants in a variety of urban, industrial, and rural areas—have contributed to identifying, and better understanding, air quality seasonality features. However, they often lack in rational explanations that could lead to more general conclusions and correlations, and be used for predictive purposes. Relevant to the present study, we note here a comprehensive survey of the environmental and ecological status in the City of Krasnoyarsk [8], and on the seasonal variation of pollutant concentration over the period of

five years using a mobile gas-analysis laboratory [1]. The study examines significant differences in seasonal air quality variations in various parts of the city aimed at identifying the role of microclimatic heterogeneity and the effects of river breeze and orographic-type circulations on urban air pollution. Studies of a similar character can also be found for a number of large cities and urban agglomerations, e.g., References [2–6].

Whilst the measurements provide indispensable information, identifying the causes and consequences of the observed phenomena and establishing some even approximate correlations with the dynamics of pollutant emission remains still a challenge. We argue that numerical simulations of space and time dynamics of air flow and pollutant dispersion, while accounting for realistic configuration of ground canopies and atmospheric conditions can fill this gap, complementing the measurements with additional information and providing a predictive tool for prognostic purposes. Some applications of the same computational software and models used in the present work can be found in References [9–12].

We consider carbon monoxide, CO, the source of which, in an urban environment, is attributed mostly to the vehicles from city traffic [3,4], far exceeding NOx and particles [1,7].

For countries with a cold climate, there is a general trend that pollution from traffic is greater in winter due to additional fuel consumption on space heating. However, the traffic distribution and its diurnal intensity usually remain the same over the whole year. This is the case for Krasnoyarsk (Russia). The measurements in various points of the city [1] show that the average traffic flows in winter and summer are quite similar. Therefore, the spatial distribution pattern of CO emission should also be similar (except for larger mean values in winter due to higher fuel consumption). However, the monitoring in the city of Krasnoyarsk showed anomalous winter and summer concentration distributions, uncorrelated with the emission data, Figure 1. At some locations, the ground CO levels in winter are almost twice higher than in summer, while at other locations the levels are almost equal.

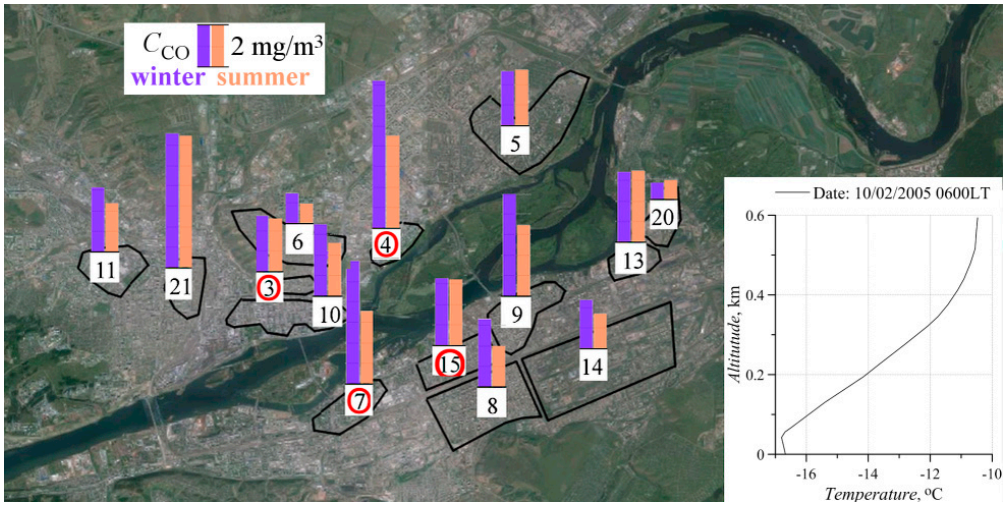

Figure 1. Measured CO concentration in different parts of the Krasnoyarsk city in the winter and in the summer seasons (data from Reference [1]), black lines indicate the measurement zones. Inset: A typical observed winter morning inversion in the area (data from Reference [8]).

The change in CO concentration distribution might be attributed to the seasonal differences in local air circulations generated by the river, surrounding heat islands and terrain orography. It is interesting to note that higher winter levels of CO are observed close to the river banks. Indeed, the observed patterns hint at a significant role of the river in the considered situation. In winter, when the ambient temperature may drop below −30 °C, the river (Yenisei) does not freeze (after the erection of a large hydro power-plant accumulation upstream). Thus, the river in winter acts as a powerful source of heat, moisture and buoyancy for the surrounding atmosphere. The authors' previous paper [9] showed that

in conditions of low or no external wind with capping inversion the convective flow generated by river and city heat islands creates a horizontal air circulation, directed toward the river at low altitudes and away from the river at higher altitudes. The estimated air velocity was up to 3 m/s near the ground.

The weather monitoring in and around Krasnoyarsk [8] shows that capping inversion of different strength often occurs in the region and prevails throughout two-thirds of the year (Figure 1 inset). In view of the above, we speculate that the anomalous local increase of pollutant concentration may be caused by the "river-breeze" effect. To test the above hypothesis and to gain more insight into the physics, we compare the winter and summer situations by means of numerical simulation.

2. Computational Details

The simulations were carried out with the in-house finite-volume BuoyFlow CFD code (TU Delft, The Netherlands) using the Reynolds-average Navier–Stokes (RANS) k-ε-θ^2 algebraic turbulent flux model [11] with the buoyancy-accounting functions for the ground boundary conditions, verified in a number of generic and real-life configurations [9–12]. The numerical method was similar to the one used in Reference [9].

The ensemble-averaged RANS conservation equations for mass, momentum, energy (in terms of the potential temperature), CO concentration in air and humidity (with neglect of the molecular terms):

$$\frac{D\langle U_i\rangle}{Dt} = -\frac{\partial \tau_{ij}}{\partial x_i} - \frac{1}{\rho}\frac{\partial \langle P\rangle}{\partial x_i} + f\varepsilon_{ij3}\left\langle U_j\right\rangle + \beta g_i\left(\langle T_v\rangle - T_{ref}\right), \tag{1}$$

$$\frac{D\langle T\rangle}{Dt} = -\frac{\partial \tau_{\theta j}}{\partial x_i}, \tag{2}$$

$$\frac{D\langle S\rangle}{Dt} = -\frac{\partial \tau_{sj}}{\partial x_i}, \tag{3}$$

$$\frac{D\langle H\rangle}{Dt} = -\frac{\partial \tau_{hj}}{\partial x_i}, \tag{4}$$

are solved in the framework of time-dependent triple decomposition mode (time-dependent Reynolds-averaged Navier–Stokes, T-RANS) [11], in which the instantaneous variable $\Phi = U_i, \Theta, H$ was split into a long-time (long-phase or ensemble) averaged field, quasi-periodic (time-filtered) deterministic motion denoted by $\langle\rangle$, and stochastic fluctuation, i.e., $\Phi = \overline{\Phi} + \langle\Phi\rangle + \varphi$. The time step was chosen to be sufficiently small (6 s) to resolve in time and space the large convective vortex structures, which play a pivotal role in the flow dynamics and pollutant transport. The equations were closed using the earlier reported 3-equation k-ε-θ^2 eddy-viscosity/algebraic flux model (EVM/AFM) [11] in which the stochastic turbulent stress tensor τ_{ij} and the turbulent heat and mass flux, $\tau_{\theta j}$ and τ_{cj}, for the unresolved ("subscale") motion were modeled respectively by

$$\tau_{ij} \equiv \overline{u_i u_j} = -\nu_t\left(\frac{\partial\langle U_i\rangle}{\partial x_j} + \frac{\partial\left\langle U_j\right\rangle}{\partial x_i}\right) + \frac{2}{3}\langle k\rangle\delta_{ij} - c_\phi\frac{\langle k\rangle}{\langle\varepsilon\rangle}\beta\left(g_i\tau_{\theta j} + g_j\tau_{\theta i}\right), \tag{5}$$

$$\tau_{\theta i} \equiv \overline{\theta u_i} = -c_\phi\frac{\langle k\rangle}{\langle\varepsilon\rangle}\left(\tau_{ij}\frac{\partial\langle T\rangle}{\partial x_j} + \xi\tau_{\theta j}\frac{\partial\langle U_i\rangle}{\partial x_j} + \eta\beta g_i\left\langle\theta^2\right\rangle\right), \tag{6}$$

$$\tau_{si} \equiv \overline{su_i} = -c_\phi\frac{\langle k\rangle}{\langle\varepsilon\rangle}\left(\tau_{ij}\frac{\partial\langle S\rangle}{\partial x_j} + \xi\tau_{sj}\frac{\partial\langle U_i\rangle}{\partial x_j}\right), \tag{7}$$

$$\tau_{hi} \equiv \overline{hu_i} = -c_\phi\frac{\langle k\rangle}{\langle\varepsilon\rangle}\left(\tau_{ij}\frac{\partial\langle H\rangle}{\partial x_j} + \xi\tau_{hj}\frac{\partial\langle U_i\rangle}{\partial x_j}\right), \tag{8}$$

where $\nu_t = c_\mu \langle k \rangle^2 / \langle \varepsilon \rangle$ is the eddy viscosity, β is the thermal expansion coefficient, f is the Coriolis coefficient and $T_v = T(1 + 0.61H)$ the virtual potential temperature. The coefficients take the commonly adopted values: $c_\mu = 0.09$, $c_\phi = 0.2$ and $\xi = \eta = 0.6$.

The terms in braces stand for the resolved time-filtered quantities, which were obtained by solving, in time and space, the transport equations for the turbulence kinetic energy (TKE) $\langle k \rangle$, its dissipation rate $\langle \varepsilon \rangle$ and the temperature variance $\left\langle \theta^2 \right\rangle$, resulting in a three-equation k-ε-θ^2 model. The effective (total) second moments (turbulent stress, heat and mass flux) consist of the resolved and sub-scale (stochastic) components, $\overline{\langle \Phi \rangle \langle \Psi \rangle} + \overline{\varphi \psi}$.

The computational domain of $40 \times 20 \times 1.5$ km^3 was discretized by 20×10^6 grid cells, clustered near the ground to keep t, e cell size in the city about $40 \times 40 \times 2$ m^3. The realistic orography was generated from GIS data; and the initial and boundary conditions are depicted in Figure 2. The buildings are assumed as the main source of the UHI (urban heat island) effect. In summer, the buildings accumulate solar radiation due to inter-reflections of sunlight. In winter, the central heating and industrial activity make buildings warmer than the surrounding ambient air [13,14].

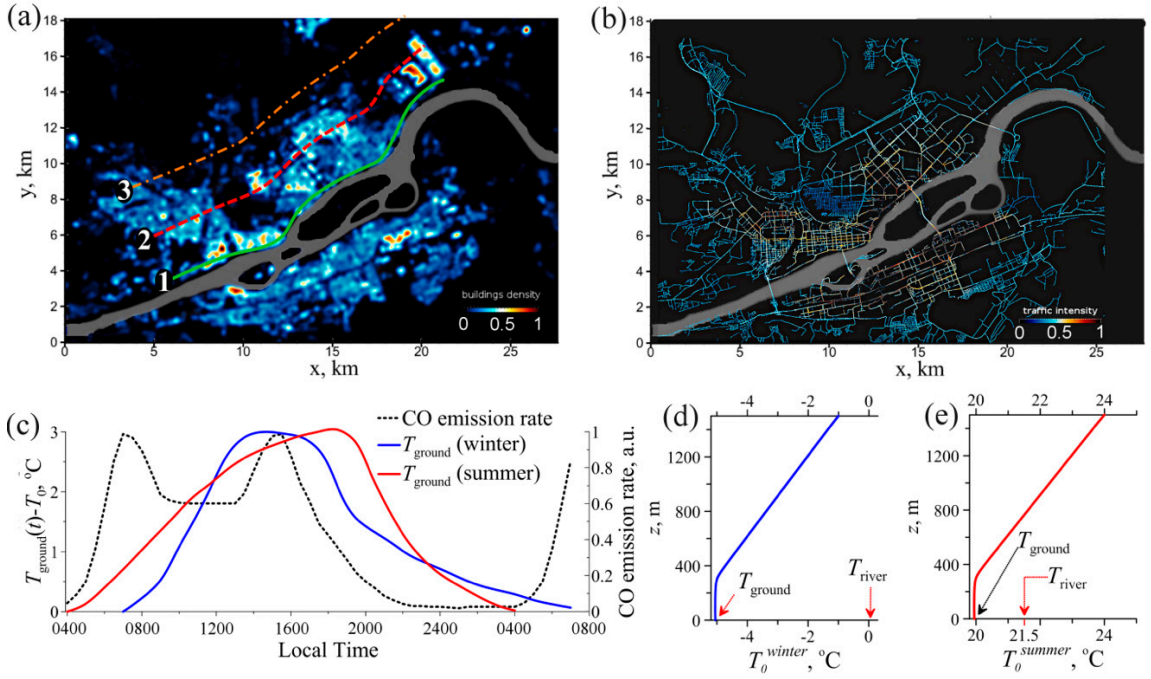

Figure 2. Krasnoyarsk urban canopy with the river Yenisei and traffic arteries. (**a**) Relative buildings density map (coloured lines show the averaging path for the statistics, see Section 3.3); (**b**) Traffic activity in different parts of the city; (**c**) Diurnal variation of temperature and concentration emission used in the simulation; (**d**,**e**) Initial temperature profiles for summer and winter cases. T_0 denotes the initial ground temperature (20 °C in the summer case and −5 °C in the winter case).

Considering the lack of detailed information on the UHI distribution over the city of Krasnoyarsk, we chose to set the magnitude of temperature anomaly over the city proportional to the density of the building. The buildings map was obtained from GIS source [15]; then each building was weighted with its height. A uniform grid with 40×40 m^2 cells was superimposed on a map of the building, and the area of each grid cell (multiplied by their heights) was computed. The UHI-induced excess ground temperature distribution was then set proportional to that map (Figure 2a) with the mean magnitude of 1 °C over the simulated terrain.

Recent measurements of traffic and CO concentration from mobile, area and major stationary sources in Krasnoyarsk [1] were used to generate a map of near-ground CO concentration, Figure 2b. The near-surface CO emission rate at the roads locations was set proportional to the local traffic flux (number of vehicles per hr.). This spatial distribution was then modulated as a function of time to reflect

the diurnal variation. The diurnal cycle of surface CO emission (Figure 2c, dotted line) was assumed proportional to the change in traffic activity (taken from Reference [8]) with two "rush-hour" peaks at 0700 LT and 1600 LT. As it is hard to correctly estimate the ratio between the CO emission intensity and traffic flux for the current conditions, the CO concentration was calculated in arbitrary units (a.u.), and then normalized. This was done by assuming that the mean simulated concentration at 10 m altitude should be equal to the mean measured surface CO concentration—taken from Reference [1]. The normalization was done separately for the summer and winter scenarios.

The initial vertical temperature profiles for both cases are shown in Figure 2d,e. For both scenarios, a ground-adjacent mixed layer was capped by inversion layer with its base set at an altitude of 300 m. The inversion strength was set to 3.3 °C/km, admittedly considerably milder than observed in winter morning conditions (shown in the inset in Figure 1). The initial profiles of turbulence model variables (k, ε, θ^2) were taken from a precursor simulation with a uniform ground heating, which we ran for some short time before the main simulation.

The diurnal variation of ground temperature (Figure 2c) was taken from the several-days averaged data from local meteorological observations in June and February. The magnitude of ground temperature diurnal variation over the city was taken to be 3 °C. In the city center, the effect of UHI (with temperature distribution shown in Figure 2a) adds about 1 °C to that baseline variation. The winter simulation was started at 0700 LT while the summer simulation at 0400 LT, reflecting the difference at the time of sunrise.

While the UHI intensity was similar for the summer and winter cases, the temperature of the river (assumed constant for the whole diurnal period) was different. For the winter case, the river temperature was set at ~0 °C (which is 5 °C higher than the surroundings), while for the summer case, the river temperature was assumed to be equal to the mean diurnal surface temperature of 21.5 °C. Thus, in winter, the river should be the source of atmospheric convection during the whole diurnal cycle, while in summer it should stabilize the ABL at the daytime and destabilize it at night [16].

The river surface velocity, obtained from precursor two-dimensional simulation of the river water flow, was used as the air velocity ground conditions, as reported in Reference [9] with the maximum velocity magnitude of 3 m/s for both simulations.

3. Results and Discussion

3.1. Seasonal Air Circulation, CO Distribution and Their Correlation

Instantaneous snapshots of volume rendering of the CO concentration (C_{CO}) at 1800 LT in Figure 3 give an impression of a typical late afternoon pollutant dispersion over the city in summer (Figure 3a) and in winter (Figure 3b). Note that the grey-scales in two figures differ, but they both show the maximum concentration in the same central downtown region, though with a markedly different distribution.

The instantaneous plots of C_{CO} late afternoon (1800 LT), shown in Figure 4, provide ample evidence for some conclusions on the typical dispersion paths across the city. The figures also contain profiles of air velocity at various locations, thus facilitating the identification and interpretation of the flow patterns and convection of the pollutants. The CO emission is clearly depicted at both parts of the city by peak CO concentration spots near the ground. For the *summer*, it can be seen that the concentration is first convected upwards from the location of emission sources and then, after reaching the inversion layer, spreads horizontally (Figure 4c). At some cross-sections (Figure 4c,d) this spreading is preferably away from the river (effectively removing the pollutant from the city), while in some other cross-sections (Figure 4a,b, the western part of the city) its preferable movement is toward the river (thus leading to accumulation of pollutant). It is interesting to note that the pollutant in some places moves over the river at 500 m altitude and then descends to a ground level and gets entrained by the flow feeding the updraft at the other side of the city (Figure 4b).

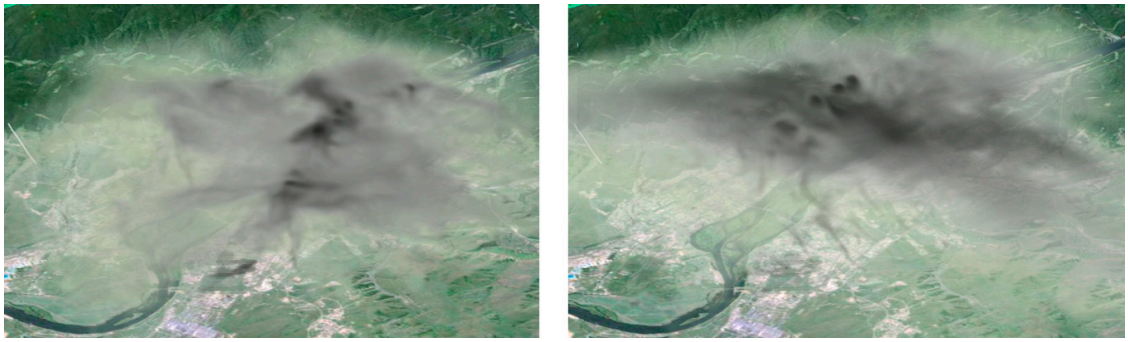

(**a**) (**b**)

Figure 3. Snapshots of instantaneous CO concentration distribution at 1800 LT. (**a**) Summer; (**b**) winter (volume rendering).

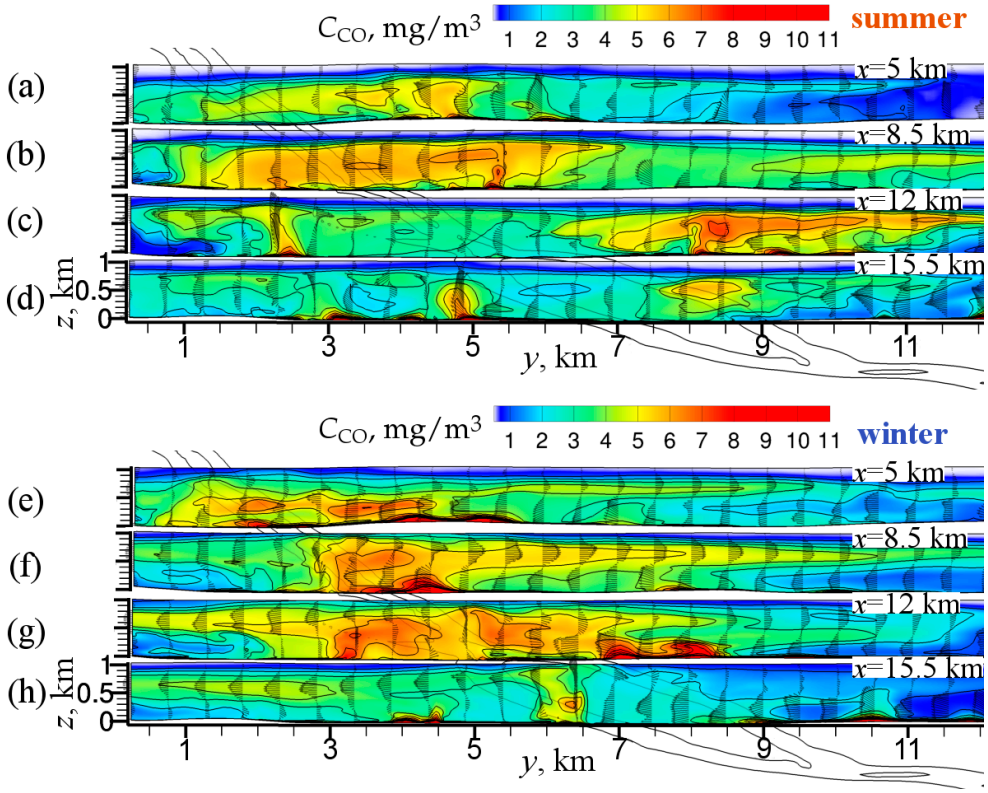

Figure 4. Instantaneous CO concentration distribution and velocity vectors in several vertical cross-sections (along the *y*-axis) across the river at 1800 LT. (**a**–**d**) Summer; (**e**–**h**) Winter.

In general, this behavior is connected to the local circulations created by UHI effect. The updraft currents are generated at the points of local maxima of surface temperature at both river banks with horizontal circulations around them. The river, which is colder than the surroundings at the daytime prohibits the spreading of local circulations to an opposite river bank at low altitudes. But at higher altitudes, the interconnections between circulations make possible the transport of pollutant to the opposite banks of the river.

The *winter* situation is quite different (Figure 4e–h). A strong circulation generated by a warm river dominates the UHI circulations. Therefore, after the emission pollutant is advected toward the river at low altitudes, it can be seen that such motion leads to a pronounced peaks in the concentration distribution near the river (Figure 4e–g). Then the pollutant gets into the main updraft above the river and lifts upward. This is reflected in a local CO concentration maximum at some altitude above the

river (Figure 4f,g). After the uplift the pollutant spreads in a horizontal direction, leaving the urban area. This spreading is more intense in winter, as already shown in Figure 3.

A plot of the mean streamlines, Figure 5, confirms striking differences between the summer and winter flow patterns. In line with our earlier findings [9], the winter conditions create large horizontal air circulation with two zones separated by the river plume. In summer, however, each side of the city acts as a separate heat island, generating its own local circulation. In summer, the air is transferred above the river at higher altitudes from one bank to another, whereas in different parts of the city that transfer may have opposite directions, as shown in Figure 5a,b. Daily-averaged horizontal velocity magnitudes in winter are several times higher than in summer.

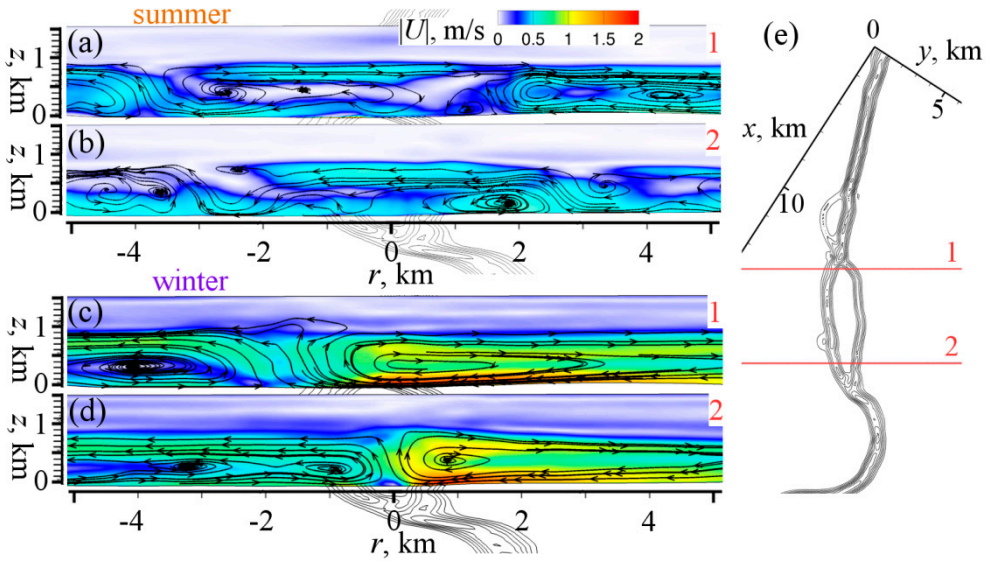

Figure 5. Streamlines and contours of the velocity magnitude in vertical cross-sections, averaged over one day of simulation. (**a**,**b**) Winter case; (**c**,**d**) Summer case; (**e**) The cross-sections positions.

The flow patterns shown in Figure 5 are well reflected in the daily-averaged CO concentration, depicted in Figure 6 in the same vertical cross-sections. In summer (Figure 6a,b), the region around the river remains relatively unpolluted, while high concentrations appear in two zones distant from the river, where the pollutant is trapped into the local recirculation zones shown by streamlines in Figure 5. In the winter scenario, the two regions of high C_{CO} merge into one, making the area close to the river highly polluted (Figure 6c). In the other cross-section (Figure 6d), the two maximum concentration regions do not merge, but both deform horizontally in the direction toward the river. A more intensive horizontal advection of C_{CO} in the winter case leads to a weaker vertical concentration flux above the city and higher mean concentrations of the pollutant near the ground surface.

More details of the CO distribution for both seasons are provided in Figure 7. In the top row, Figure 7a,b show the instantaneous CO concentration values and contours for summer (left) and winter (right) in a horizontal cross-section at 50 m above the ground, whereas Figure 7c and d in the bottom row present their 24 hours' time-averaged distribution in the same plane. Evidently, as shown in particular by the instantaneous snapshots, despite the similar emissions and ground CO concentrations, air circulation patterns and the time-averaged distributions (Figure 7a,b) in summer and winter are quite different. In summer, two maxima of concentration appear above the opposite river banks, but in winter these maxima merge over the river leading to an increase in the net concentration values. In the suburbs, the opposite is observed. In winter, the pollutant is advected towards the river, and unpolluted air is entrained from around the city. Another winter peculiarity is a highly heterogeneous pollutant distribution with several "hot spots".

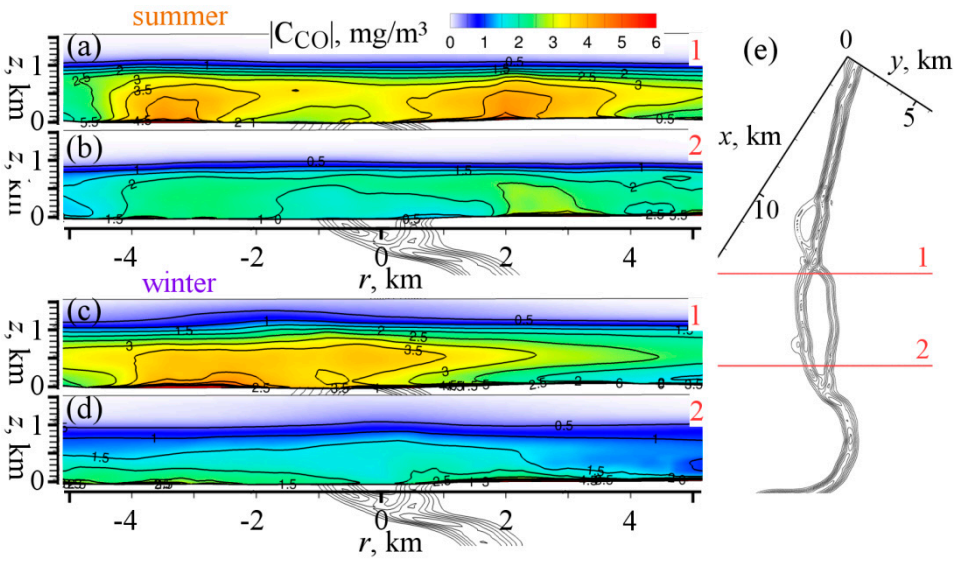

Figure 6. Daily-averaged CO concentration fields in vertical cross-sections. (**a**,**b**) Summer case; (**c**,**d**) Winter case; (**e**) The cross-sections positions.

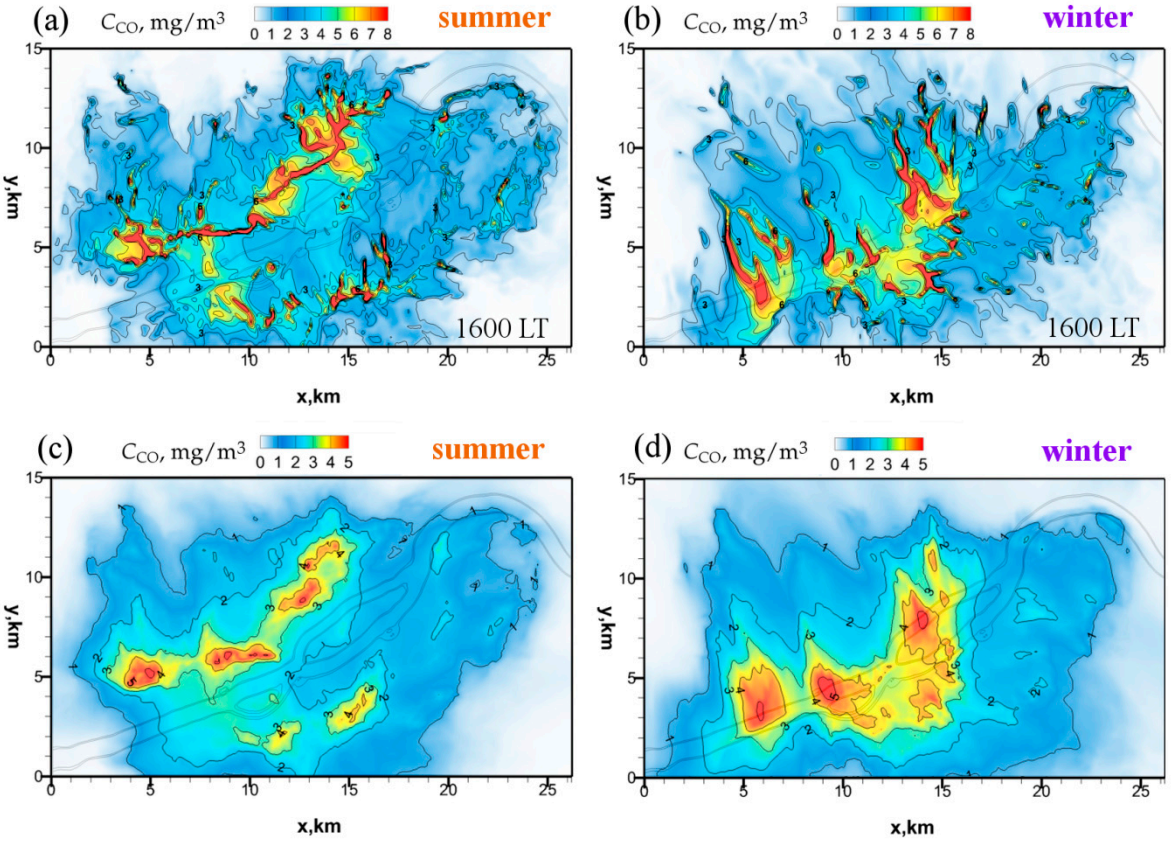

Figure 7. CO concentration distribution in a horizontal cross-section at 50 m above the ground (**a**,**b**) Instantaneous (1600 LT) plots; (**c**,**d**) Daily averaged plots; (**a**,**c**) Summer case; (**b**,**d**) Winter case.

The peculiar CO distribution pattern with multiple local high-concentration spots reflects a complex flow and vortex structures that develop over the city due to the inversion-capped river-induced thermal convection. The instantaneous fields, Figures 4 and 7a,b show the common convective patterns over suburbs, where the ground temperature is more or less uniform, with streaky structures (roll-convection) closer to the city (for more details and vortex generation mechanism see Reference [9]). In winter,

these streaks are attracted toward the river, where in summer they are directed toward the center of each part of the UHI. It is evident that the river in the winter case has a large overall effect on the flow structure, intensifying horizontal air motion. In the summer case, the river acts as a barrier, separating two parts of the flow from each other.

3.2. Vortical Structures and Their Role in CO Dispersion

The above-mentioned structure pattern is evident in the instantaneous distribution of CO concentration (Figure 7a,b). Two horizontal "line" vortex structures with axes nearly parallel to the river, containing most of the pollutant, is observed in summer. These structures correspond to the urban heat island centers, but their alignment with a river suggests that in this case, the river also plays a role in shaping the overall circulation and pollutant distribution.

In the winter case, the observed streaks of concentration with axes normal to the river reflect closely the trumpet-like vortical structures originating from baroclinic interaction of the horizontal ground-temperature gradient and gravity vector, identified in authors' previous study of vortex dynamics during a diurnal winter cycle over the same city domain [9]. Similar structures are known for cold air outbreak events over the sea or lake shore [17–19] or in laboratory studies of mixed convection [20].

An impression of the typical vortex patterns in summer and winter is given in Figure 8. In the summer case, Figure 8a, distinct river-parallel rolls are clearly identifiable along the river, with less orderly multiple vortices (attributed to convective cells) populating the neighboring areas of both sides. In winter, the field is characterized by conspicuous multiple river-normal trumpet-like vortical streaks over the two river banks at lower altitudes. It is interesting to note how the temperature is gradually increasing along with these streaky structures as they are moving closer to the river. Above the river, some convective cells are evident above which there are horizontal vortex rings generated from the interaction of an updraft with an inversion layer. At higher altitudes, river parallel structures are observed. These vortex rolls are characterized by elevated air temperature, due to the accumulation of heat taken from the updraft, are moved away from the river with the main horizontal circulation flow.

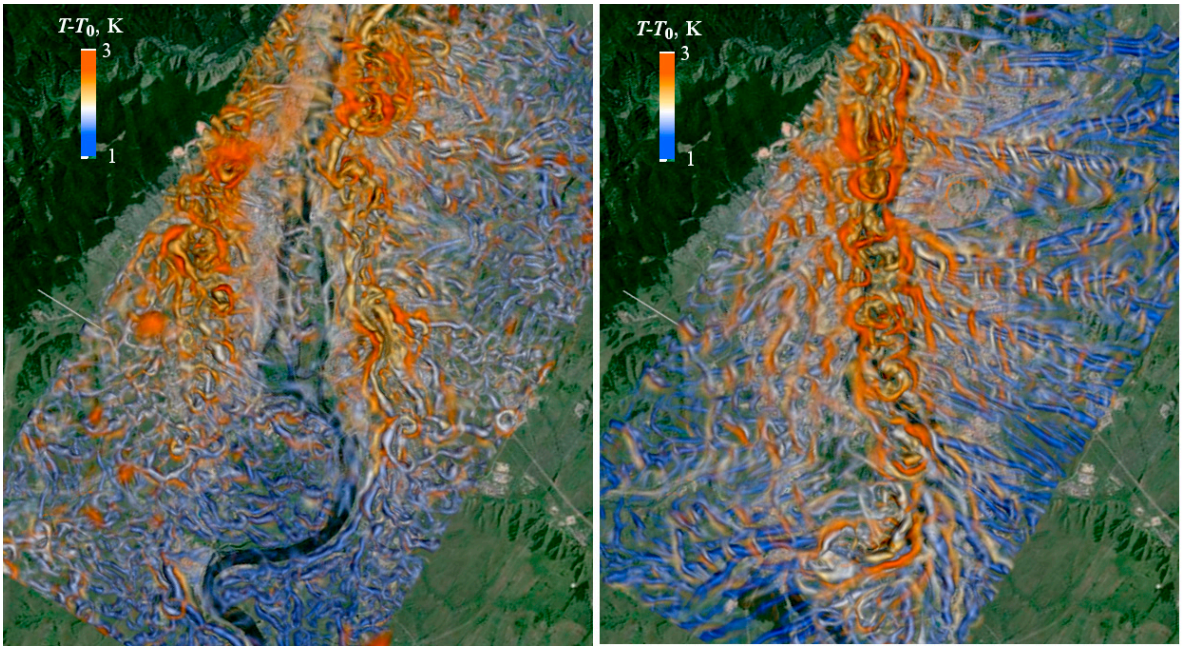

Figure 8. Instantaneous vortex structure over the city (1600 LT), visualized by the Q-criterion colored by the temperature. (**a**) Summer case; (**b**) Winter case.

3.3. Quantitative Analysis of the Averaged Air Velocity and CO Concentration

For a more quantitative analysis, we consider averaging of the instantaneous fields over the lines of constant distance from the river, as shown in Figure 2a (denoted as 1, 2 and 3). The first line goes close to the river, the second through the middle of the city, and the third through the suburbs. The CO concentration profiles averaged over the vertical planes along these lines at three time-instances, Figure 9, illustrate the evolution of the pollutant concentration field. The results show a significant difference between the winter and summer cases reflecting the overall pictures, shown in Figures 4–7. In the winter case, the concentration above the river is the highest throughout the whole domain height, diminishing gradually with the distance from the river. In the summer scenario, the concentration reaches its maximum over the middle of the city, especially at the near ground altitudes. However, in the upper part of the domain, above 200 m altitude, the concentration above the river is close to that above the middle of the city.

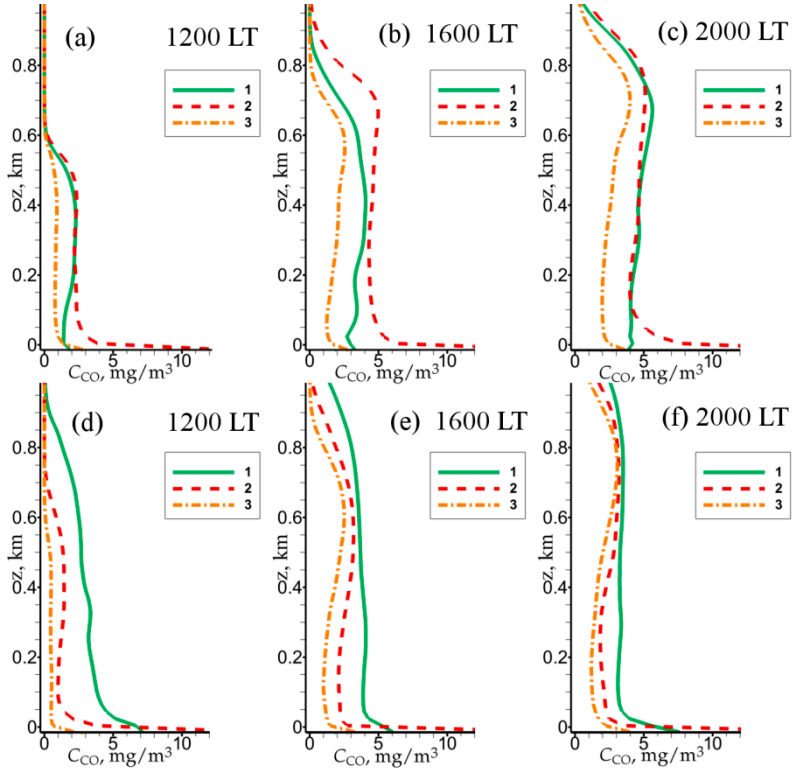

Figure 9. Vertical profiles of CO concentration, averaged over the cross-sections (along the lines 1, 2, 3 indicated in Figure 2a), at different diurnal phases. (**a**–**c**) Summer case; (**d**–**f**) Winter case.

The time evolution of the profiles shows how the concentration is accumulated in some regions of the simulation domain. The vertical transport of CO is most significant above the river during winter (Figure 9d–f), where strong river plume transports the pollutant upward. However the mean flow circulation, shown in Figure 5, transports CO back to the city at higher altitudes, which is reflected in the appearance of a concentration peak above the city and suburbs (Figure 9e,f), noticeable in the midday and in the evening.

In the summer case, the main updraft forms above the middle of the city, leading to a strongest vertical heat flux at that location. The interaction of the updraft with the inversion layer at this point leads to a sharper vertical gradient of concentration in the upper part of the domain than in the winter case.

The horizontal velocity profiles at different distances from the river are shown in Figure 10. It can be seen that summer and winter flow patterns are quite different. In the winter case (Figure 10d–f),

at all three distances from the river the velocity profiles behave similarly, with negative (i.e., toward the river) values in the lower part of the domain and positive (i.e., away from the river) values in the upper part. As the ground heating is intensified (Figure 10d,e) the velocity maximum appears at low altitudes (~50 m), but when the heating starts to decrease (Figure 10f) the velocity maximum is shifted upward, probably due to an inertial effect of the circulation generated during the day.

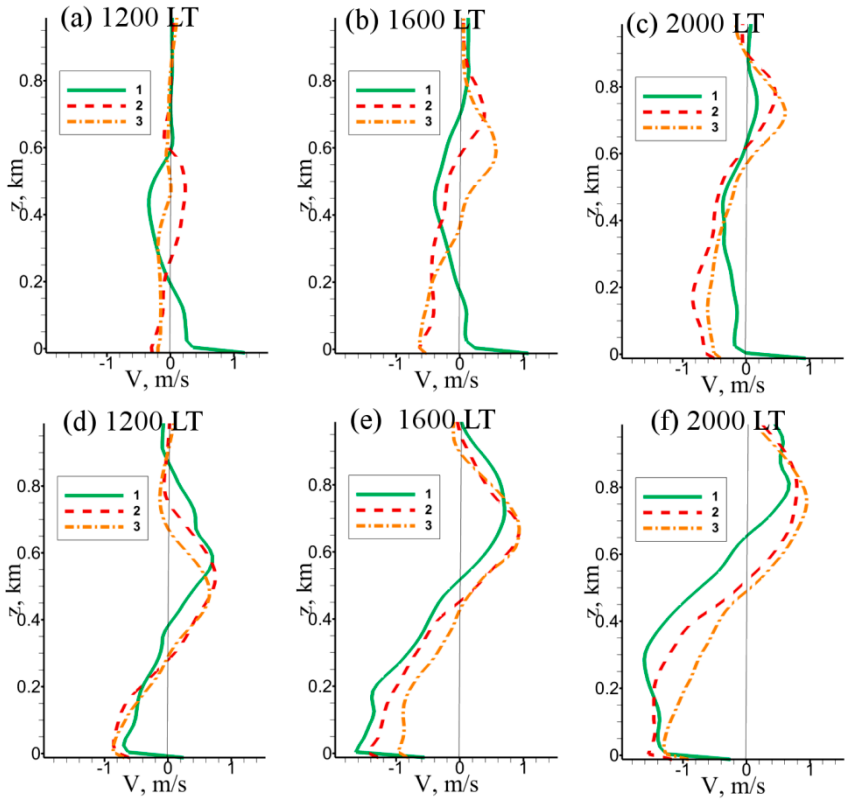

Figure 10. Vertical profiles of horizontal velocity (*y*-component), averaged over the cross-sections (along the lines 1, 2, 3 indicated in Figure 2a), at different diurnal phases. (**a**–**c**) Summer case; (**d**–**f**) Winter case.

In the summer case (Figure 10a–c), the airflow in the lower part of the domain is directed toward the warmest part of the city. In the beginning of the day (Figure 10a), the flow from the river is the strongest (with a velocity of about 0.35 m/s), but as the heating continues, this flow weakens, and eventually becomes inverted at the end of the day (Figure 10c). This behavior is associated with the diurnal variation of the ground temperature compared to the temperature of the river. The horizontal temperature gradient at the bottom is forcing the air to flow in its direction through a baroclinic mechanism, but as this gradient weakens in the evening, the residual inertial forces of the airflow may reverse the mean velocity direction. In the upper part of the domain, in summer, we also see that evening flow direction is changed above the river (Figure 10c). While throughout the first part of the day the air moves toward the river at higher altitudes (opposite to the flow above the city), in the evening the velocity profiles above all three monitoring locations are similar, showing the air movement away from the river at higher altitudes.

In general, the mean horizontal velocity magnitude in winter is about two times larger than in summer (2 m/s compared with 1 m/s), which indicates that effect of the river and the central updraft on the mean flow is quite significant.

The temperature, turbulent kinetic energy and heat flux profiles for the peak heating intensity (1600 LT) are shown in Figure 11. The temperature distribution for the summer and winter cases (Figure 11a,d) show some differences. In winter, stronger horizontal advection leads to a modification

of the temperature profiles above the city. Warmer air, spreading horizontally from the updraft, increases the temperatures below the inversion. This effect may act, to some extent, as a reinforcement mechanism for stable stratification and damping of buoyancy.

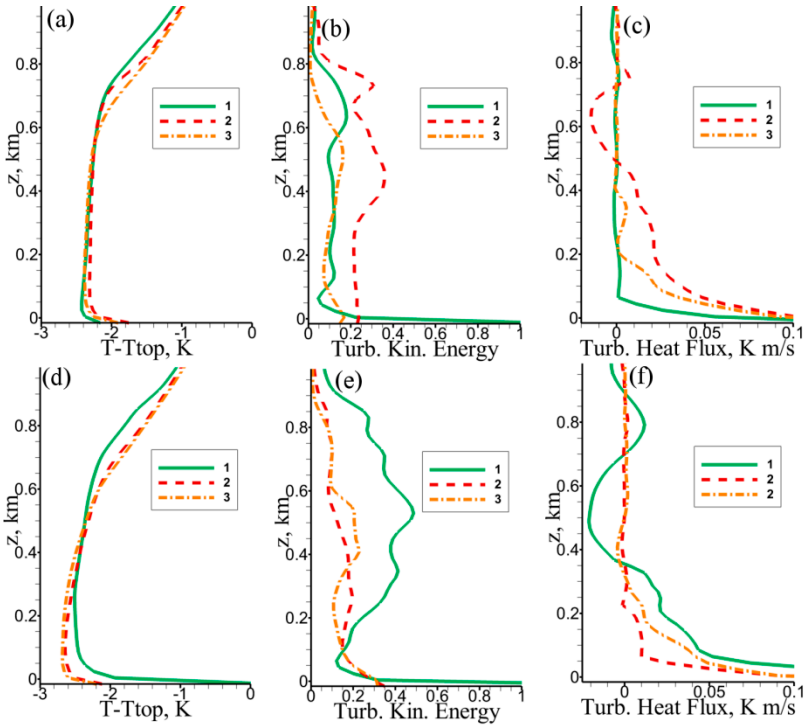

Figure 11. Vertical profiles, averaged over the cross-sections (along the lines 1, 2, 3 indicated in Figure 2a), at different diurnal phases. (**a**,**d**) Temperature; (**b**,**e**) Turbulence kinetic energy; (**c**,**f**) Vertical turbulent heat flux; (**a**–**c**) Summer case; (**d**–**f**) Winter case.

In the summer case, the temperature profiles look similar to the common penetrative convection of a mixed layer. All three profiles at different locations are very close to each other. The turbulence kinetic energy (TKE) profiles (Figure 11b,e) show the highest values above the most intensively heated areas (middle of the city in summer and the river in winter). It is noticeable that quite large values of TKE are observed in the upper part of the domain above the river in the winter case, which should be a consequence of the strong updraft there, accumulating the buoyancy energy from the surrounding areas. As expected, at the instant, shown in Figure 11 (late afternoon, 1600 LT), strong damping of the TKE is noticeable only in the inversion layer.

The sensible (turbulent) heat flux profiles (Figure 11c,f) are quite similar for two cases, reflecting the intensity of local heating from the ground. That means that the mid-city profile in the summer is similar to the above-the-river profile in the winter. It is interesting to note that in the winter case, the suburb profile shows higher flux values than the mid-city profile. That may be explained by the fact that strong horizontal advection is damping the vertical motion that drives the vertical heat flux.

3.4. Temporal Evolution of the Flow and Concentration Fields

To investigate the temporal evolution of the concentration fields, four points were selected at which the vertical profiles of flow fields were saved at every time step of the simulation. The selected points are “3”, “4”, “7”, and “15” from Figure 1. Two of the points (“3” and “4”) are located at the left bank of the river and the other two on the right bank. The evolution of the concentration and velocity fields near the surface is shown in Figure 12. The difference in the behavior of the fields between different points is quite evident. At points “3” and “15” (Figure 12a,d) the concentration for the summer and winter cases shows a remarkably similar behavior featured by gradual growth toward

the 1600 LT. This behavior reflects the emission intensity (Figure 2c), thus meaning that convection does not play a significant role at this location. However, it is interesting that the peak value from the morning "rush hour" at 0700 LT is present at point "3" and is much less pronounced at point "15" for both the summer and winter cases. The velocities at these points have similar magnitudes in summer and winter (Figure 12e,h). At point "3" the morning velocity direction is toward the river for both cases, then, at about 1200 LT in summer the velocity reverses its direction due to the growth of the UHI-induced circulation. In winter, the flow retains its direction toward the river and its velocity growth with the increase of ground convective motion during the daytime and decreases in the evening.

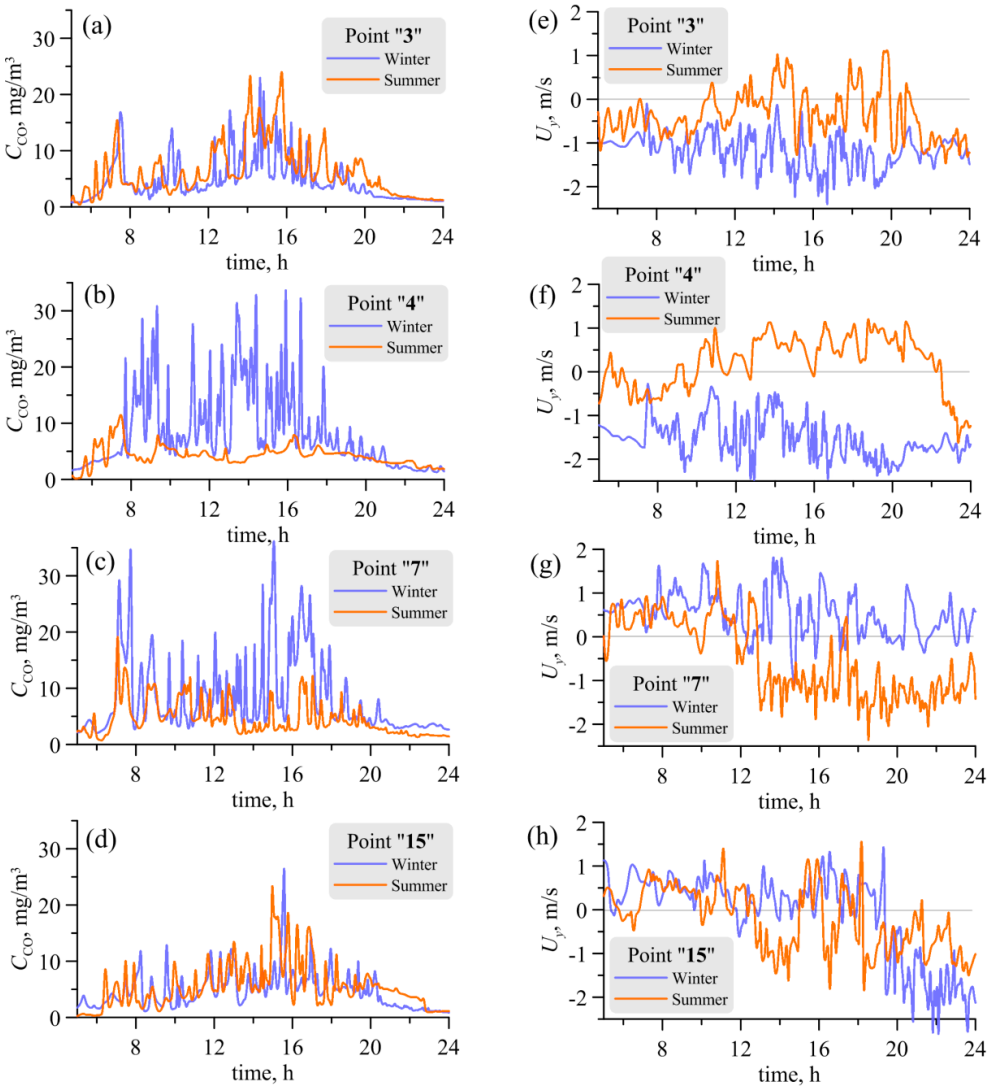

Figure 12. Modeled fields temporal evolution plots near the ground (10 m altitude) for several points (shown in Figure 1). (**a**–**d**) Concentration; (**e**–**h**) Horizontal velocity (river-normal component).

At point "15" located on the other river bank, the flow has the same morning behavior as for point "3" (except for the sign of velocity). But after 2000 LT the winter flow experiences the change in direction, presumably reflecting the change in local circulation shape or the local fluctuation of the updraft position.

Two other points show significant differences between the summer and winter simulations. At point "7" the concentration-time plot (Figure 12c) has a shape very similar to that of the emission intensity, but in winter the peak values are about twice larger than in summer—which could be

attributed to a weaker vertical flux in winter in the morning hours (due to later sunrise), and a weaker horizontal velocity in the later time (the latter can be seen from Figure 12g). It is interesting to note that after 1200 LT in summer, a change of velocity direction appeared at location "7" from toward-to away-from-the-river. This effect should be associated with the moment when the river surface temperature becomes lower than the surroundings, thus creating a land-river breeze.

The point "4" show the most significant difference between the summer and winter cases. For summer, the time profile of concentration is similar to the one from point "7". But the winter case shows very high values in between the emission peaks, which indicates the dominant role of convection bringing the pollutant to this point from elsewhere. This is confirmed by the high values of horizontal velocity in the direction toward the river (Figure 12f) at this point.

For further analysis we consider some results at two other characteristic points, "4" and "15". It is first noted that point "15" shows very similar behavior of time evolution of ground surface concentration fields for the summer and winter, while point "4" shows the largest difference.

The time evolution of vertical profiles of CO concentration is shown in Figure 13. For point "15" (Figure 13c,d) it can be seen that at about 0900 LT for both scenarios, some CO traces appeared just below the inversion layer. The pollutant can arrive there from some updraft that is located nearby, dragging the air horizontally at low altitudes. The vertical (advective) flux of concentration at the same point (Figure 14c,d) shows very low values in the morning. But after 1200 LT strong spikes in the vertical flux, coinciding with the peak values in the concentration profiles for the summer case, mean that at this point intermittent vertical motions (from the updrafts of convective cells) are dominant. For the winter case (Figure 14d), a strong vertical transfer is also present at this point, but for a much shorter period of time (from 1500 LT to 2100 LT). For the winter case, a faster decrease of concentration levels is evident in the upper part of the flow where a strong horizontal circulation moves the air away from the river, thus leading to faster cleaning of the flow below the inversion.

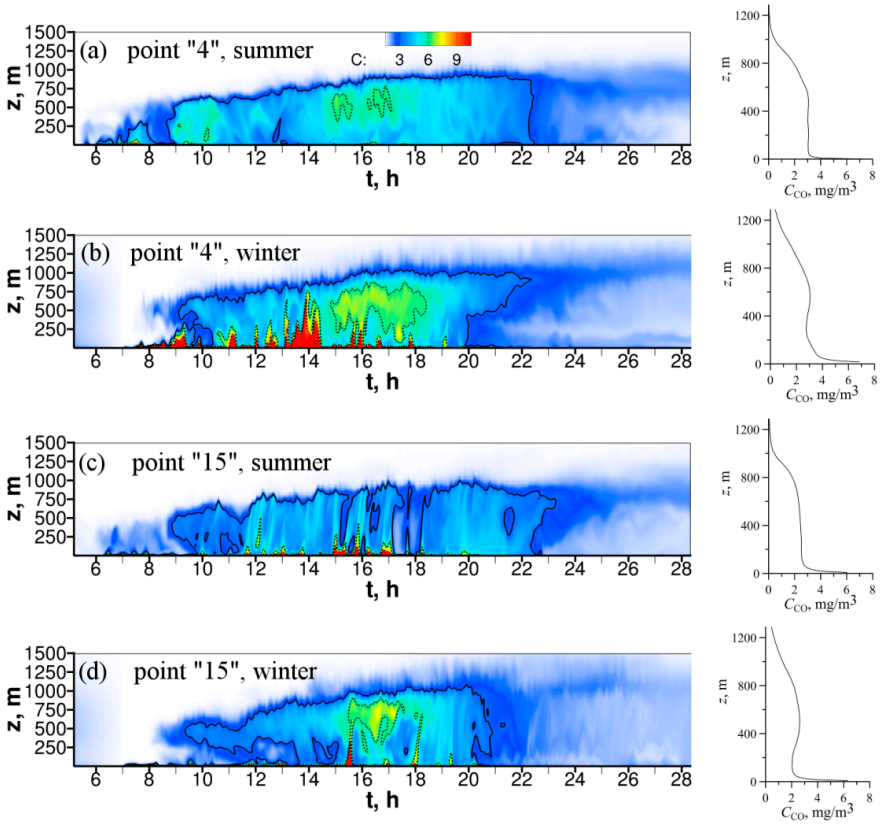

Figure 13. Temporal evolution of CO concentration fields (left) and daily-averaged concentration profiles (right) for several points (shown in Figure 1). (**a**,**c**) Summer case; (**b**,**d**) Winter case.

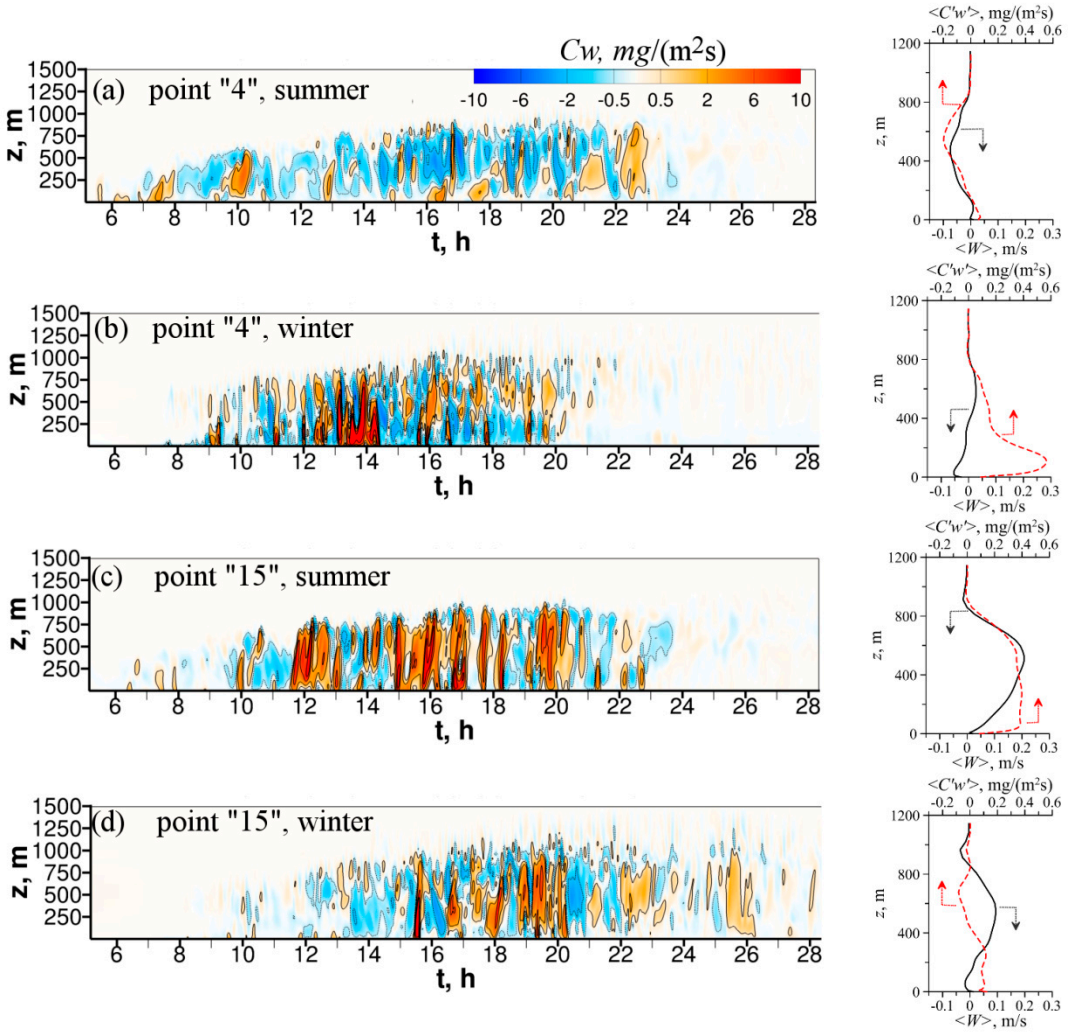

Figure 14. Temporal evolution of vertical advection intensity (*Cw*) (left) and daily-averaged profiles of vertical velocity and vertical turbulent concentration flux <*c*′*w*′> (right) for several points (shown in Figure 1). (**a**,**c**) Summer case; (**b**,**d**) Winter case.

For point "4" in the summer case (Figure 13a), a gradual growth of concentration profile is evident. This is accompanied by low values of the vertical advection intensity. It is interesting to note that the vertical advective flux is prevalently negative, indicating at a downdraft at this point. In the winter case (Figure 13b), the situation is different. Very strong spikes of high concentration are seen in the lower part of the flow correlated with vertical advection maxima (Figure 14b).

The daily-averaged vertical turbulent CO concentration flux profiles are shown together with mean vertical velocity in the right panel of Figure 14. In summer, the behavior of turbulent flux is similar to the behavior of mean vertical velocity; while in winter (especially for point "4") there is no such correlation. At point "4" (Figure 14b) strong positive vertical turbulent concentration flux is present below 400 m in altitude where the mean vertical velocity is negative. That might indicate that the main source of turbulent fluctuations in the winter case is not a vertical, but the mean horizontal velocity.

The intensity of horizontal advection is depicted in Figure 15. It shows that the main cause of a difference between the CO concentration values in summer and winter at point "4" is the horizontal concentration flux (Figure 15c,d). In the summer case, it is directed from the river toward the city, thus bringing along a clean air from the river. But in winter the flux is directed in the opposite direction, therefore transferring contaminated air from the city toward the river. The magnitude of horizontal flux in winter case is also much higher.

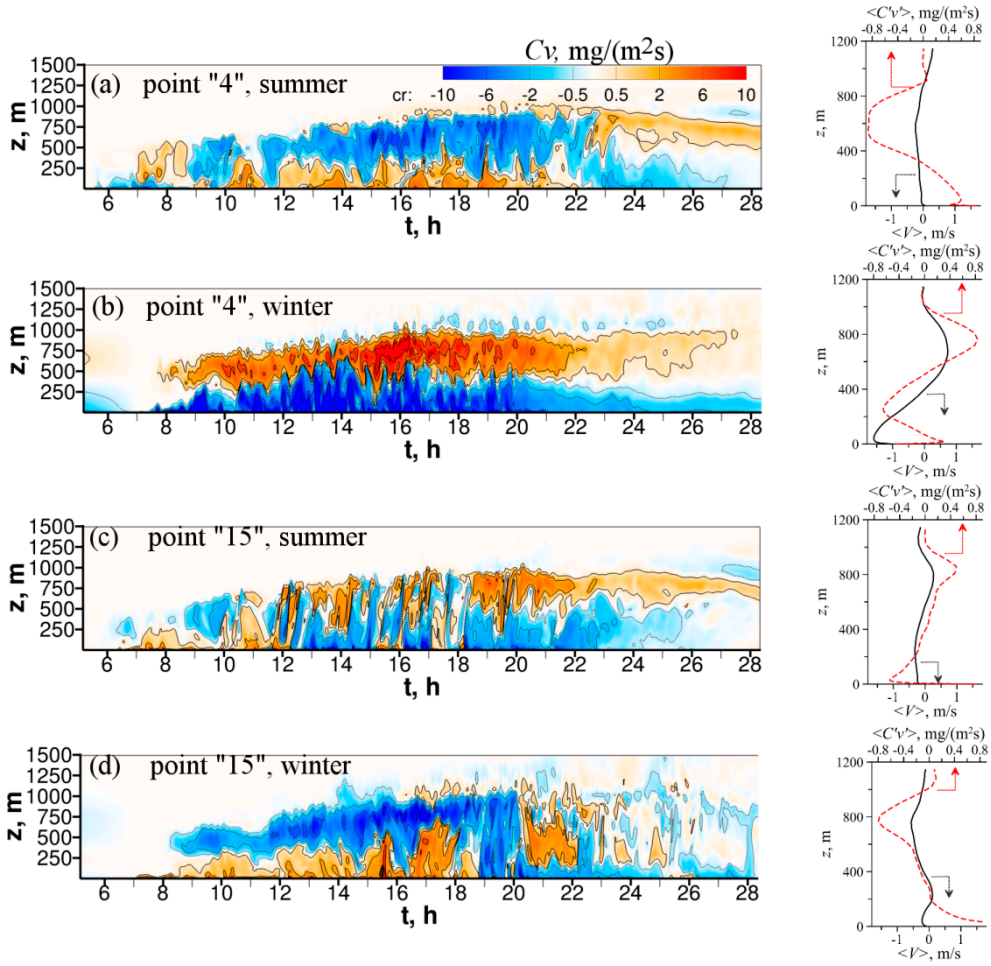

Figure 15. Temporal evolution of horizontal (in the direction across the river) advection intensity (Cv) and daily-averaged profiles of horizontal velocity (in the direction of the river) and horizontal turbulent concentration flux $<c'v'>$ (right) for several points (shown in Figure 1). (**a**,**c**) Summer case; (**b**,**d**) Winter case.

It is interesting to note the change of direction of the horizontal flow at point "15" in winter (Figure 15d) this change happened when the ground started to cool in the second part of the day. This change may be connected to some dynamical transition between the convection modes of the flow. Due to this non-stationary effect, the air starts to move away from the "warm" river, thus locally breaking the horizontal circulation.

3.5. A Note on Flow Stability

To close discussion on the role of river-induced convection in the pollutant dispersion, we address the issue of flow stability briefly, by analyzing the time evolution of the gradient Richardson number:

$$Ri = \frac{\beta g \frac{\partial T}{\partial z}}{\left(\frac{\partial U}{\partial y}\right)^2 + \left(\frac{\partial V}{\partial x}\right)^2}, \tag{9}$$

which is convenient and easy to compute. However, as widely discussed in the literature [21–23], this may not be the best option in the fully mixed layer where the potential temperature is close to being uniform. Nevertheless, at least in the surface layer, it can give some indication of the stability threshold commonly defined by $Ri \approx 0.21$.

The time evolution of R_i at locations "4" and "15" for the summer and winter scenarios is shown in Figure 16. It can be seen that in summer (Figure 16a,c) the altitude of the instability threshold (defined by $Ri \approx 0.21$) grows in the morning significantly faster than in winter. This can be explained by the generation of more intense updrafts above the UHI in summer while in winter the horizontal convection created by the river is dominant in the morning hours leading to more stable flow conditions. However, this intense horizontal winter circulation leads to the faster growth of the inversion layer in winter and a higher mean vertical heat flux, which is shown in Figures 10 and 11. In the evening, this circulation leads to a faster decay of vertical convection above the city, thus re-stabilizing the flow. The values of ($Ri < 0.21$) can be seen at the near ground levels in the winter simulation at some points (Figure 15b) indicating the reestablishing of the inversion and stabilization of the flow. In the summer simulations, this effect is much less pronounced. In the real situation, radiative cooling (not accounted in the present simulations) should play an important role in reestablishing stability in the night time. However, the horizontal circulation from the river acts in a similar way, intensifying a negative heat flux from the cold ground into the atmosphere.

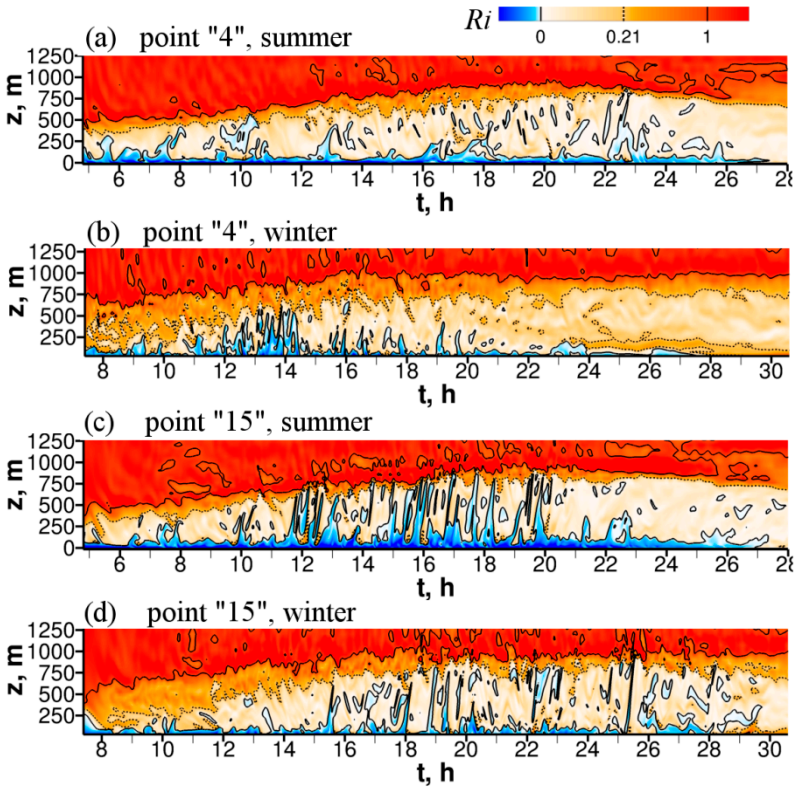

Figure 16. Temporal evolution of Richardson number distribution for several points (shown in Figure 1). (**a**,**c**) Summer case; (**b**,**d**) Winter case.

3.6. Comparison with Observations

To our knowledge, only averaged ground-level measurements are available at particular points of the city that show the difference between the summer and winter pollutant concentration distribution for Krasnoyarsk [1].

No vertical profiles for the same observational period are available of relevant properties (e.g., temperature, velocity and concentration) that could help to validate and verify the computational approach, applied here. However, to provide at least some quantitative justification, Figure 17 shows a comparison of the measured (reported in Reference [1]) and computed daily averaged CO concentration in summer and winter at a number of locations over the whole domain considered.

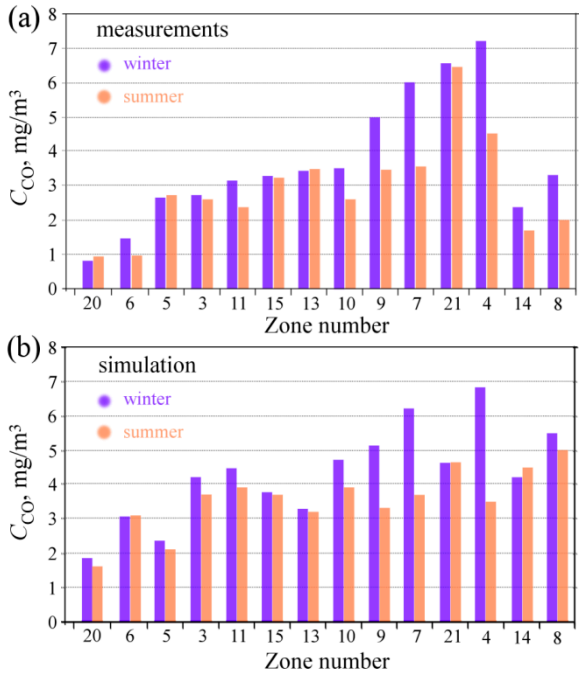

Figure 17. Comparison of the measured [1] and simulated CO concentrations (averaged over a day) at various locations in the city (indicated in Figure 1). Blue. Winter; orange, summer. (**a**) Measurements; (**b**) Simulation (at 10 m altitude). Zone numbers from Figure 1.

The sequence of measuring points in Figure 17 (from left to right) is chosen to show a monotonic increase in the measured concentration (apart from the last two locations), and thus to provide an impression of the CO variation over the city. Despite some noted differences in the absolute values of the measured and simulated data, an agreement can be considered as satisfactory.

The simulations data show the same trend as the measurements, for both the winter and summer case—qualitatively exposing the difference between the two seasons. While the absolute values of simulated and measured concentrations differ, there is a similarity in the locations where the maximum concentration difference between the summer and winter cases occur. The maximum seasonal differences in the mean CO concentration were observed in locations "4", "7", "9", "10". The same holds for the current simulation. These points (shown in Figure 1) are located close to the river banks. Thus, the influence of the change in circulation pattern between the summer and winter should be maximal at these points providing the highest difference in concentration between the seasons.

The absolute values of this seasonal concentration variation for the mentioned points are markedly similar between the simulation and the measurements. This leads to the conclusion that the river effect is indeed strong enough to be one of the main reasons for the observed seasonal variation.

Despite marked differences in the absolute values of CO concentration at some locations (e.g., points "14", "8", and "21") considering some unavoidable uncertainties in the input data, boundary conditions and scenarios, as well as some uncertainties in the measurements, the simulation results can be regarded as satisfactory.

4. Conclusions

The three-dimensional time-dependent RANS (T-RANS) simulations of convective boundary layer and pollutant dispersion in the region of the city of Krasnoyarsk for windless winter and summer conditions confirmed the field observation that despite very similar pollutant emission from city traffic throughout the year, the patterns of pollutant concentration differ markedly for the two scenarios. It is shown that one of the causes of the seasonal difference is the river Yenisei flowing through the city, which governs air circulation and net heat and mass transfer. In winter, the "warm" river acts as

a source of thermals, entrains air from both sides into horizontal motion towards the river at lower altitudes, transporting pollutants toward the city center. In summer, the "cool" river acts as a barrier blocking air motion from one part of the city to another, creating two separate convective flows above the north and south parts of the city. The mean concentration is shown to be higher close to the river in winter than in summer in accord with the field observations.

Despite some uncertainties in the input data and some simplifications of the real configuration (e.g., using equivalent roughness to model urban canopy and a sinusoidal instead or irregularly periodic daily variation of the ground temperature), agreement with the field measurements can be considered as satisfactory. Thus, the results provide sufficient confidence in the here applied computational T-RANS approach for predicting dynamics and trends of pollutant dispersion in real environmental situations with authentic terrain complexity and imposed specific meteorological conditions.

Author Contributions: Methodology, K.H.; software, M.H.; formal analysis K.H. and M.H.; writing—original draft preparation, M.H. and K.H.; writing—review and editing, K.H.; visualization, M.H.

Funding: This research was funded by the Russian Science Foundation, grant number 17-77-10116.

Conflicts of Interest: The authors declare no conflict of interest.

References

1. Mikhailuta, S.V.; Taseiko, O.V.; Pitt, A.; Lezhenin, A.A.; Zakharov, Y.V. Seasonal variations of air pollutant concentrations within Krasnoyarsk City. *Environ. Monit. Assess.* **2009**, *149*, 329–341. [CrossRef] [PubMed]
2. Cattani, G.; di Bucchianico, A.D.M.; Dina, D.; Inglessis, M.; Notaro, C.; Settimo, G.; Marconi, A. Evaluation of the temporal variation of air quality in Rome, Italy from 1999 to 2008. *Ann. Ist. Super Sanità* **2010**, *46*, 242–253. [PubMed]
3. Miao, Y.; Hu, X.M.; Liu, S.; Qian, T.; Xue, M.; Zheng, Y.; Wang, S. Seasonal variation of local atmospheric circulations and boundary layer structure in the Beijing-Tianjin-Hebei region and implications for air quality, AGU Publ. *J. Adv. Model. Earth Syst.* **2015**, *7*, 1602–1626. [CrossRef]
4. Yao Té, Y.; Jeseck1, P.; Franco, B.; Mahieu, E.; Jones, N.; Paton-Walsh, C. Seasonal variability of surface and column carbon monoxide over the megacity Paris, high-altitude Jungfraujoch and Southern Hemispheric Wollongong stations. *Atmos. Chem. Phys.* **2016**, *16*, 10911–10925. [CrossRef]
5. Pandey, B.; Agrawal, M.; Singh, S. Assessment of air pollution around coal mining area: Emphasizing on spatial distributions, seasonal variations and heavy metals, using cluster and principal component analysis. *Atmos. Pollut. Res.* **2014**, *5*, 79–86. [CrossRef]
6. Zhao, X.; Zhang, X.; Xu, X.; Xu, J.; Meng, W.; Pu, W. Seasonal and diurnal variations of ambient PM2.5 concentration in urban and rural environments in Beijing. *Atmosph. Environ.* **2009**, *43*, 2893–2900. [CrossRef]
7. Wang, T.; Xie, S. Assessment of traffic-related air pollution in the urban streets before and during the 2008 Beijing Olympic Games traffic control period. *Atmosph. Environ.* **2009**, *43*, 5682–5690. [CrossRef]
8. Khlebopros, R.G.; Taseyko, Y.D.; Ivanova, S.V.; Mikhailuta, S.V. *Krasnoyarsk. The Ecological Studies*; Siberian Federal University Press: Krasnoyarsk, Russia, 2012; p. 130.
9. Hrebtov, M.; Hanjalić, K. Numerical study of winter diurnal convection over the city of Krasnoyarsk: Effects of non-freezing river, undulating fog and steam devils. *Bound.-Layer Meteor* **2017**, *163*, 469–495. [CrossRef]
10. Kenjereš, S.; Bevrnja, A.; Žilić, A.; Hanjalić, K. *Modelling Pollutant Dispersion over a City in a Hilly Terrain under Initially Stable and Neutral Stratification*; Hanjaić, K., Miyauchi, T., Borello, D., Hadžiabdić, M., Ventiruni, P., Eds.; Turbulence, Heat and Mass Transfer 8, Begell House Inc.: New York/Wallingsford, UK, 2015; pp. 719–722.
11. Kenjereš, S.; Hanjalić, K. Combined effects of terrain orography and thermal stratification on pollutant dispersion in a town valley: A T-RANS simulation. *J. Turbul.* **2002**, *3*, 026. [CrossRef]
12. Hanjalić, K.; Hrebtov, M. Ground Boundary Conditions for Thermal Convection Over Horizontal Surfaces at High Rayleigh Numbers. *Bound.-Layer Meteor* **2016**, *160*, 41–61. [CrossRef]
13. Giridharan, R.; Kolokotroni, M. Urban heat island characteristics in London during winter. *Sol. Energy* **2009**, *83*, 1668–1682. [CrossRef]
14. Miles, V.; Esau, I. Seasonal and spatial characteristics of urban heat islands (UHIs) in northern West Siberian cities. *Remote Sens.* **2017**, *9*, 989. [CrossRef]
15. OpenStreetMap Buildings Data. Available online: https://www.osmbuildings.org/ (accessed on 10 June 2019).

16. Hathway, E.A.; Sharples, S. The interaction of rivers and urban form in mitigating the urban heat island effect: A UK case study. *Build. Environ.* **2012**, *58*, 14–22. [CrossRef]
17. Liu, A.Q.; Moore, G.W.K.; Tsuboki, K.; Renfrew, I.A. A high-resolution simulation of convective roll clouds during a cold-air outbreak. *Geophys. Res. Lett.* **2004**, *31*, 1–4. [CrossRef]
18. Zurn-Birkhimer, S.; Agee, E.M.; Sorbjan, Z. Convective structures in a cold air outbreak over Lake Michigan during Lake-ICE. *J. Atmos. Sci.* **2005**, *62*, 2414–2432. [CrossRef]
19. Young, G.S.; Kristovich, D.A.; Hjelmfelt, M.R.; Foster, R.C. Supplement to rolls, streets, waves, and more. *Bull. Am. Meteorol. Soc.* **2002**, *83*, 1001. [CrossRef]
20. Yu, C.H.; Chang, M.Y.; Lin, T.F. Structures of moving transverse and mixed rolls in mixed convection of air in a horizontal plane channel. *Int. J. Heat. Mass. Transfer.* **1997**, *40*, 333–346. [CrossRef]
21. Webb, E.K. Vanishing potential temperature gradients in strong convection. *Q. J. R. Meteorol. Soc.* **1958**, *84*, 118–125. [CrossRef]
22. Townsend, A.A. Natural convection in the earth's boundary layer. *Q. J. R. Meteorol. Soc.* **1962**, *88*, 51–56. [CrossRef]
23. Deardorff, J.W.; Willis, G.E. The free-convection temperature profile. *Q. J. R. Meteorol. Soc.* **1967**, *93*, 166–175. [CrossRef]